Georgantzia E, Finney C, Robinson A and Kashani MM (2024) Modeling Nonlinear Stress–Strain Behavior of 6000 Series Aluminum Alloys under Cyclic Loading. ASCE Journal of Materials in Civil Engineering. 36(6): 04024133. https://ascelibrary.org/doi/abs/10.1061/JMCEE7.MTENG-17314

Modeling nonlinear stress–strain behaviour of 6000 series aluminum alloys under cyclic loading

Evangelia Georgantzia

Teaching Fellow

Email: e.georgantzia@soton.ac.uk

Address: Room 3019, Building 178,

University of Southampton

Boldrewood Innovation Campus, Burgess Road, Southampton, SO16 7QF

United Kingdom

Charles Finney

Undergraduate Student

Email: cf1n20@soton.ac.uk

Address: Building 178,

University of Southampton

Boldrewood Innovation Campus, Burgess Road, Southampton, SO16 7QF

United Kingdom

Andrew Robinson

Facility Manager

Email: a.robinson@soton.ac.uk

Address: National Infrastructure Laboratory (NIL), Building 178,

University of Southampton

Boldrewood Innovation Campus, Burgess Road, Southampton, SO16 7QF

United Kingdom

Mohammad M. Kashani

Associate Professor

Email: mehdi.kashani@soton.ac.uk

Address: Room 4019, Building 178,

University of Southampton

Boldrewood Innovation Campus, Burgess Road, Southampton, SO16 7QF

United Kingdom

Modeling nonlinear stress–strain behaviour of 6000 series aluminum alloys under cyclic loading

Abstract

Prior studies examining the nonlinear material properties of 6000 series aluminum alloys have predominantly concentrated on analyzing the stress-strain characteristics of these materials under monotonic tensile loading. Limited research has been conducted on their behavior under cyclic loading conditions. To address these gaps, a series of monotonic tensile and variable increasing amplitude cyclic loading tests were conducted on coupons made from 6082-T6, 6063-T6 and 6060-T5 aluminum alloys. The experimental results revealed that as strain amplitude increases the material showed isotropic strain hardening. This combined with the adequate hysteretic energy dissipation capacity demonstrate their potential advantage to be used as in structural components in earthquake prone regions. The experimental results are used to calibrate the material parameters of the uniaxial Giuffrè-Menegotto-Pinto constitutive model to be able to predict the nonlinear stress–strain behaviour under monotonic and cyclic loading. Furthermore, using fiber element modeling in OpenSees software, employing a modified Giuffrè-Menegotto-Pinto model, the flexural buckling performance of 6082-T6 aluminum alloy columns are analyzed. The results are compared with existing experimental and finite element data, demonstrating the accuracy of the model in predicting the flexural buckling behavior.

Introduction

Over the last twenty years, the 6000 series aluminum alloys have attracted considerable attention in the construction sector due to their advantageous properties. These alloys are renowned for their low weight and high strength-to-weight ratio, making them ideal for tall buildings and large structures. Moreover, their resistance to corrosion and long-lasting durability make them suitable for applications needing minimal maintenance. An important feature is their excellent extrudability, enabling the creation of intricate shapes that effectively distribute both tensile and compressive stresses, especially in critical structural areas. Considering environmental sustainability, the recyclability of aluminum alloys plays a crucial role in material choices. Additionally, their lightweight quality and flexibility expand their usability in regions prone to earthquakes, where structural elements, including dissipative components, undergo significant displacement cycles. In seismic conditions, the performance of these elements

relies on their shape and the way the material behaves under stress, as emphasized in previous studies (Nip et al. 2010; Shi et al. 2011).

Numerous studies have investigated the performance of 6000 series aluminum alloys subject to static loading, leading to the establishment of various constitutive models (Baehre 1966; Steinhardt et al. 1983; Guo et al. 2007; De Matteis et al. 2012; Yujin et al. 2013). However, research on their cyclic behavior remains limited (Georgantzia et al. 2021a). Specifically, Hopperstad et. Al. (1995a) performed cycling experiments on 6060-T4 and 6060-T5 coupon specimens. These tests involved applying both constant and varying strain amplitudes, reaching up to 1.2%. They modified Chaboche's cyclic plasticity model (1989) to account for the Bauschinger effect observed in 6060-T4 alloy. In another research (Hopperstad et al. 1995b), the researchers conducted biaxial cycling experiments, including both proportional and non-proportional conditions. They extended the constitutive model to account for the impact of strain range and load path dependency on material hardening behavior. However, the strain amplitudes of these tests was <2%, which did not fully elucidate hardening behavior of the material. To address this issue, Dusicka and Tinker (2013) conducted experiments to investigate the hysteretic behavior of 6061-T6/511 coupon specimens under constant strain amplitudes ranging from 2% to 4%. Their findings indicated a marginal rise in cyclic softening, indicating its suitability for seismic retrofitting purposes. More recently, Guo et al. (2018) conducted monotonic and cyclic tests up to 4% strain amplitudes on 6082-T6 and 7020-T6 aluminum alloys, proposing a new constitutive model for the hysteretic behavior of 6082-T6 aluminum alloy based on monotonic curves and the reduction factor method.

This paper investigates the nonlinear stress-strain characteristics of 6000 series aluminum alloys under cyclic loading experimentally. Particularly, coupon specimens made from 6082-T6, 6063-T6 and 6060 alloys are subjected to cyclic loading up to 6.5% strain amplitude. Monotonic tensile tests are also conducted, and the obtained stress–strain curves are compared with the cyclic envelope curves to determine the influence of the cyclic loading on the structural performance. The experimental results are utilised to calibrate the material parameters of uniaxial Giuffrè-Menegotto-Pinto (Giuffrè 1970; Menegotto and Pinto 1973) constitutive model. Comparisons between the experimental responses and the corresponding ones predicted based on the calibrated model are made. Finally, fiber element modeling studies on the flexural buckling performance of 6082-T6 aluminum alloy columns were performed to verify further the recommended model values.

Experimental programme

The experimental investigation was performed at the Testing and Structures Research Laboratory (TSRL) within the School of Engineering at the University of Southampton. The experimental program comprised two sets of tests including monotonic tensile tests and cyclic coupon tests, aimed to investigate the stress-strain behavior under both monotonic and cyclic loading conditions for 6082-T6, 6063-T6, and 6060-T5 aluminum alloys.

Physical and mechanical properties of the examined aluminum alloys

Magnesium and silicon are the primary alloying elements of 6000 series aluminum alloys, forming magnesium silicide (Mg2Si) through solid solution. This unique composition enables outstanding precipitation-hardening capabilities. These alloys undergo a solution heat treatment process, involving heating semifinished or finished products to a specific temperature and maintaining that temperature for a sufficient duration, allowing the alloying elements to dissolve into the material. This is followed by rapid cooling (called quenching) to keep the elements in solution so that they may be the basis of precipitation hardening upon natural, i.e., in room temperature or artificial, i.e., in a furnace, aging. In the latter case, the nature, size and volume fractions of the hardening precipitates determine the level of mechanical properties of the aluminum alloys (Kaufman 2000). 6082-T6, 6063-T6 and 6060-T5 alloys were chosen to be investigated herein as they are the most commonly used 6000 series alloys. Table 1 presents the nominal chemical composition of the three examined alloys as reported from the manufacturer (aalco 2022). This table indicates differences in the chemical compositions which result in different mechanical properties and thus different structural behaviour. Particularly, the addition of a large amount of manganese in the relatively new 6082-T6 alloy controls the grain structure forming a strong alloy. The 6082-T6 is known as structural alloy and tends to replace its older counterpart 6061-T6 alloy in many highly stressed structural applications. However, it is difficult to produce complicated extruded shapes using 6082-T6 alloy because the surface finish is not as smooth compared to 6063-T6 and 6060-T5 alloys. 6063-T6 which is commonly referred to as an architectural alloy and 6060-T5 are higher strength alloys and readily suited for welding. Both alloys are mostly used to produce intricate extrusions for architectural applications.

Geometry of test specimens

18 coupon tests were performed to assess the stress-strain response of 6082-T6, 6063-T6, and 6060-T5 aluminum alloys subject to monotonic and cyclic loading. Specifically, three monotonic tensile tests and three cyclic tests were conducted for each alloy. The coupons extracted from tubular specimens with a thickness of 3.3 mm, machined to meet the geometric requirements outlined in EN ISO 6892-1 (CEN 2009), as illustrated in Fig. 1(a) are used to perform the monotonic tensile tests. The same tubular specimens were used to make the coupons for cyclic tests. The geometry of the cyclic coupons was according to ASTM E606-04 standards (ASTM 2017) (Fig. 1(b)). It is noteworthy that the specimens' surface preparation was performed in a manner that had a minimum influence upon the variability in the exhibited nonlinear response. This was achieved by consistently machining the specimens to be as smooth and uniform in surface finish (in the gauge region) as feasible in line with the ASTM E606-04 standard (ASTM 2017). Furthermore, the gauge length of the coupons for cyclic tests was intentionally reduced compared to those monotonic specimens. This precautionary measure aimed to prevent early failure due to compression-induced buckling.

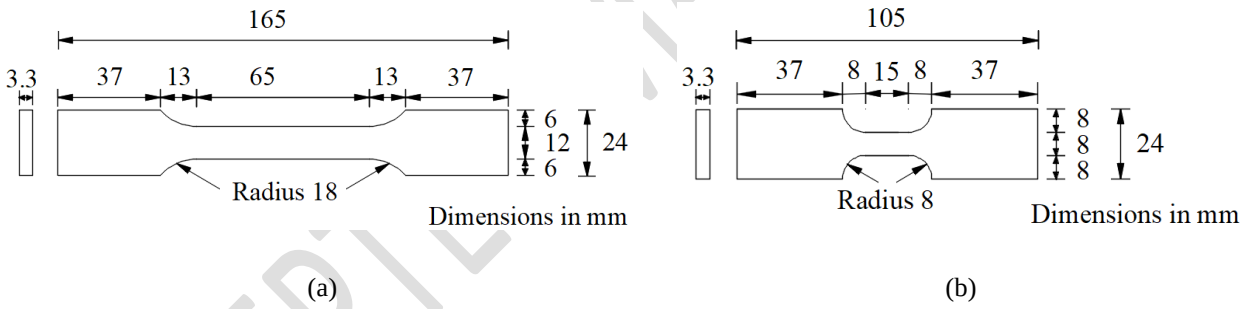

Fig. 1. Geometry of coupon specimens; (a) monotonic tensile tests and (b) cyclic tests.

Tests setup and loading protocol

Following the machining process, each coupon was placed between the grips of a 250 kN Instron testing machine and subjected to monotonic tensile loading at a rate of 0.2 mm/min, following EN ISO 6892-1 (CEN 2009) standards, until reaching fracture. Additionally, a precisely calibrated extensometer with a 50 mm gauge length was affixed to the central necked portion of every coupon to record longitudinal strains throughout the tests (refer to Fig. 2).

Fig. 2. Monotonic tensile test setup.

The procedure of the cyclic tests was similar to monotonic tests using the same machine. However, due to the smaller gauge length of the coupon specimens, an extensometer with a 12.5 mm gauge length was employed to measure longitudinal strains (see Fig. 3(a)). A symmetrical load history with two-cycle reversed strain, reaching up to 6.5% amplitude as depicted in Fig. 3(b), was applied. This loading protocol, similar to the one employed by Kashani et al. (2013), facilitated the investigation of nonlinear cyclic behavior at high strain levels, typical in regions with medium to high seismic risk (Mander et al. 1994).

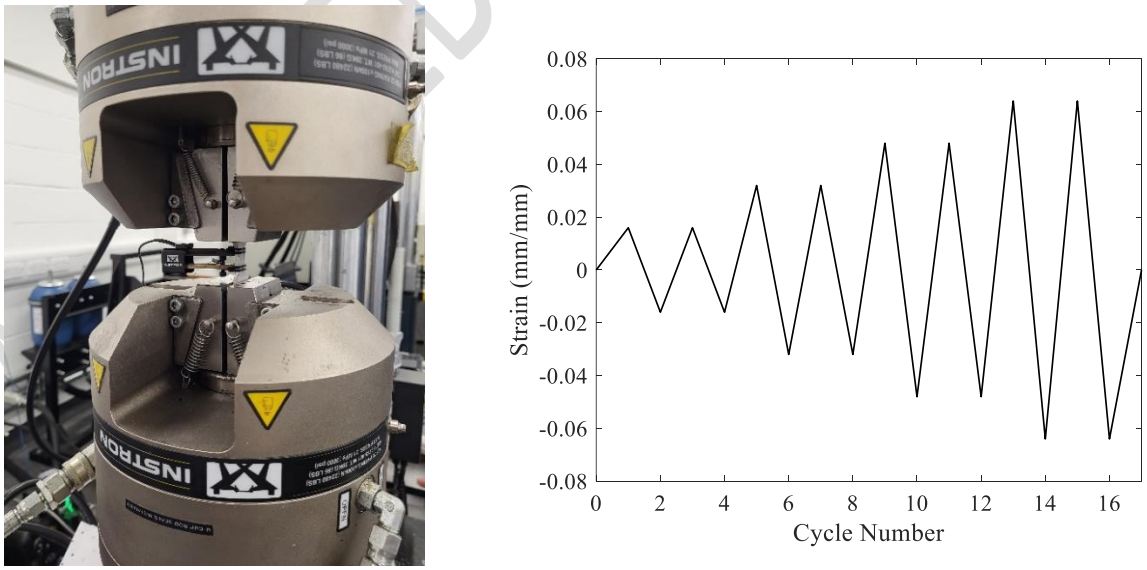

(a) (b)

Fig. 3. Cyclic tests; (a) setup and (b) loading protocol.

Experimental results

Tensile tests under monotonic loading

All coupon test specimens failed ductile with deceptive necking around the fractured section. Table 2 presents the measured mechanical properties, comprising Young's modulus (E), the 0.1% proof stress ($\sigma_{0.1}$), the 0.2% proof (yield) stress ($\sigma_{0.2}$), the ultimate tensile stress (σ_u), the corresponding strain at ultimate tensile stress (ε_u), the strain at fracture (ε_f), and the strain hardening exponent (n) as defined in Equation (1) (Hill et al., 1960; Ramberg and Osgood, 1943). In addition the $\sigma_u/\sigma_{0.2}$, defined at strain hardening ratio, for each tested coupon is also reported in Table 2. It can be seen that 6082-T6 aluminum alloy exhibited more strain hardening behavior since the $\sigma_u/\sigma_{0.2}$ value reached at 112%.

$$n = \frac{\ln 2}{\ln\left(\frac{\sigma_{0.2}}{\sigma_{0.1}}\right)} \tag{1}$$

where $\sigma_{0.1}$ and $\sigma_{0.2}$ are the stresses at 0.1% and 0.2% residual strains.

The labeling system used employed for the coupon samples denotes the specific aluminum alloy type, the type of test conducted, and its corresponding number. For instance, the term "6082-T6-M1" signifies a coupon sample made from 6082-T6 aluminum alloy subject to monotonic tensile loading. In Fig. 4, the experimental stress–strain curves are displayed, while Figs. 5(a) and 5(b) showcase the 6082-T6-M1 and all other specimens after tensile fracture subject monotonic tensile loading. Fig. 4 illustrates that the stress-strain plot of the 6082-T6 aluminum alloy displays a continuous rounded curve without a sharply defined yield point, consistent with findings in relevant studies (Georgantzia et al. 2022a; 2022b).

Table 2 Material properties obtained from monotonic tensile tests.

Specimen	E (MPa)	$\sigma_{0.1}$ (MPa)	$\sigma_{0.2}$ (MPa)	σ_u (MPa)	ε_u (%)	ε_f (%)	n	$\sigma_u/\sigma_{0.2}$
6082-T6-M1	66638	258	264	296	9.18	13.68	31.84	112%
6082-T6-M2	60182	260	267	299	7.93	16.13	26.95	112%
6082-T6-M3	73081	261	269	302	8.43	13.50	22.40	112%
6063-T6-M1	66323	322	325	337	6.99	11.39	69.37	103%
6063-T6-M2	62716	323	326	337	7.50	12.60	74.72	103%
6063-T6-M3	63488	323	326	338	6.90	12.05	75.66	104%
6060-T5-M1	67434	302	306	316	6.80	9.44	50.79	103%
6060-T5-M2	64862	301	306	316	6.79	9.38	46.69	103%
6060-T5-M3	65094	302	306	315	7.34	11.32	60.69	103%

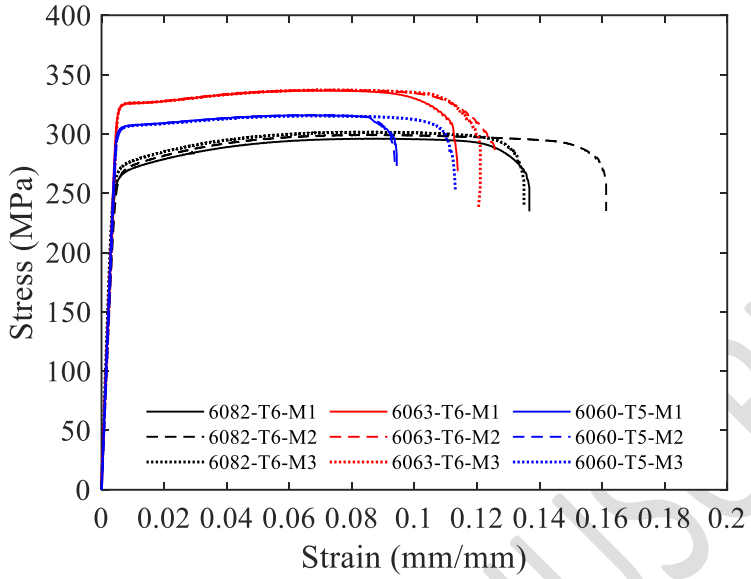

Fig. 4. Stress–strain curves obtained from the monotonic tensile tests.

(a) (b)

Fig. 5. Monotonic tensile tests; (a) 6082-T6-M1 coupon after tensile fracture and (b) all coupons after monotonic tensile testing.

Cyclic tests with increasing amplitudes

The results of cyclic tests are depicted in Figs. 6–8, where positive values represent tension and negative values represent compression. The experimental hysteretic loops exhibit robustness, indicating acceptable nonlinear cyclic

behavior and ample energy absorption capability in all tested aluminum alloys. The limited gauge length of the tested coupons effectively minimized buckling, ensuring no degradation in compressive strength during the tests. Furthermore, the second cycle of each strain demand level displayed minimal cyclic degradation, closely resembling the response observed in the initial cycle.

Beyond the yield strain, there was a combined kinematic and slight isotropic hardening response. To assess the impact of cyclic loading on material behavior, monotonic tension envelopes were also illustrated in Figures 6–8. It was assumed that the monotonic compressive response mirrored the tensile response, a presumption in line with a similar study by Kashani et al. (2013). Both tension envelope curves, under monotonic and cyclic loading, followed a similar trend, although the latter exhibited slight strain hardening.

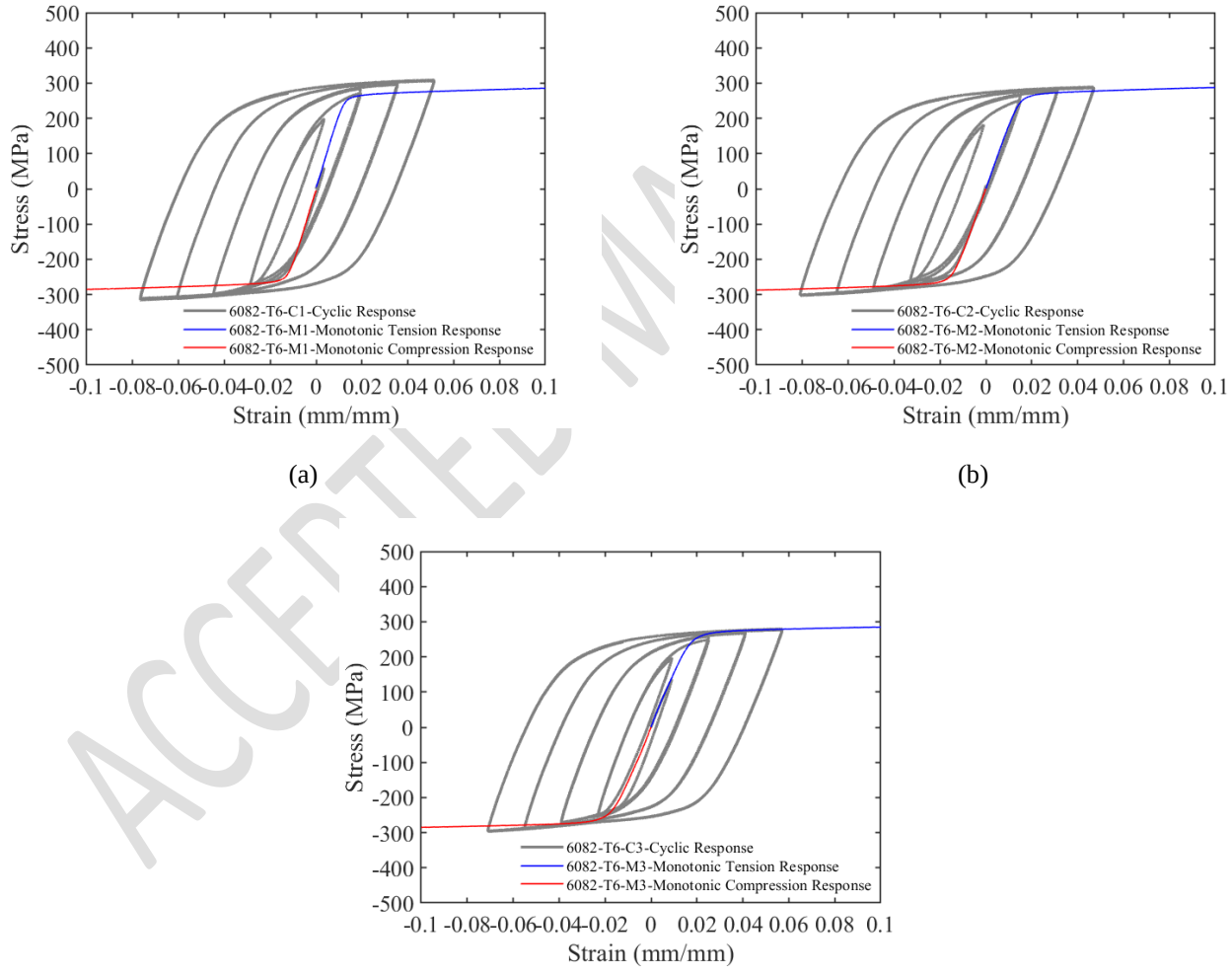

Fig. 6. Stress–strain curves obtained from the cyclic tests for 6082-T6 aluminum alloy.

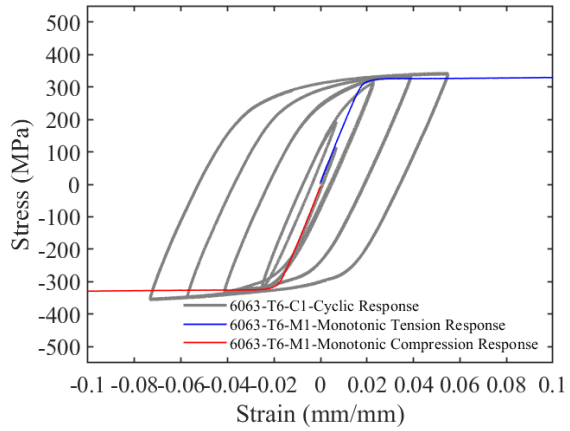

(a)

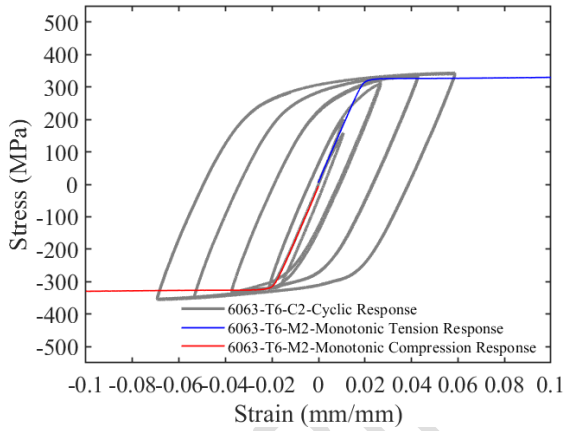

(b)

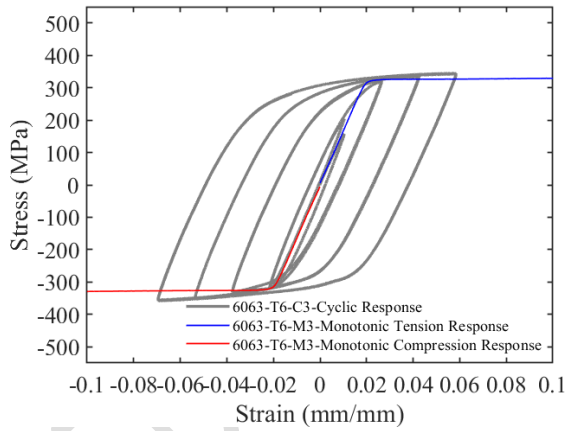

(c)

Fig. 7. Stress–strain curves obtained from the cyclic tests for 6063-T6 aluminum alloy.

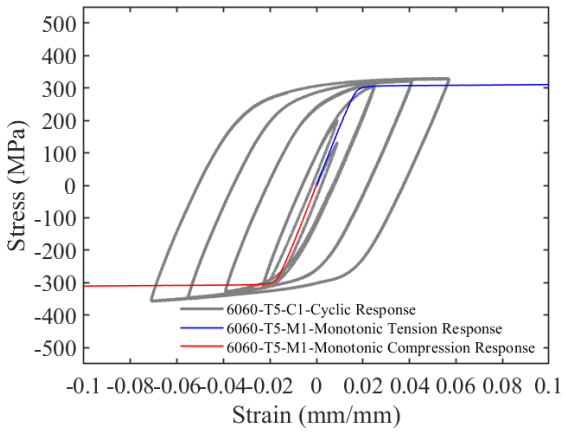

(a)

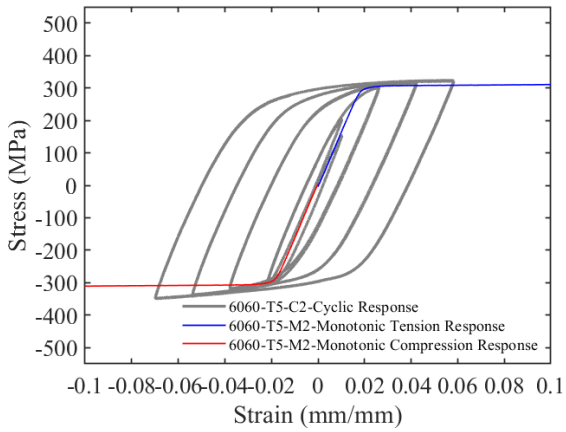

(b)

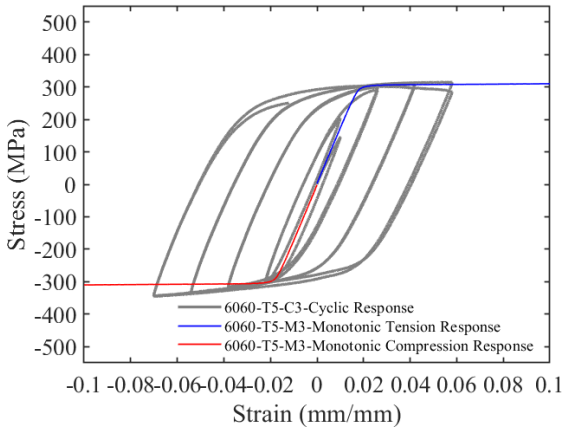

(c)

Fig. 8. Stress–strain curves obtained from the cyclic tests for 6060-T5 aluminum alloy.

Aiming to quantify and compare the cyclic energy dissipation capacity of the studied aluminum alloys, the total hysteric energy of the coupons under cyclic loading was normalised by the elastic energy of their counterparts under monotonic tensile loading and was plotted for each half cycle as shown in Fig. 9. It should be noted that the normalised hysteretic energy values were taken as the average values amongst the three material tests conducted for each studied alloy. It appears that for all studied alloys the normalised hysteretic energy increases gradually with the accumulation of cycles. However, the 6082-T6 which is the most ductile alloy, presents higher hysteretic energy dissipation capacity by 1.34 and 1.58 times more than 6063-T6 and 6060-T6 alloys, respectively.

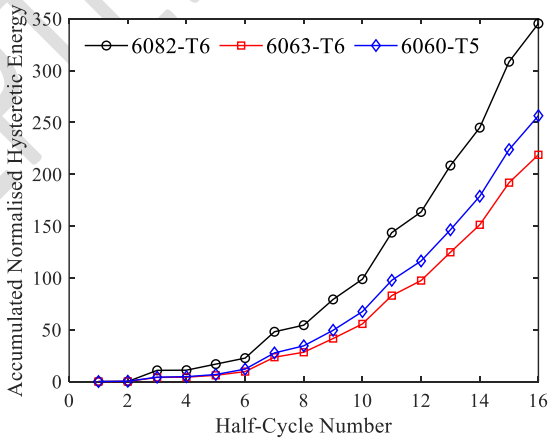

Fig. 9. Accumulated normalised hysteretic energy of the examined aluminum alloys.

Modeling of nonlinear stress–strain behaviour under monotonic tensile loading

Description of the constitutive model

The Giuffrè-Menegotto-Pinto (GMP) model (Menegotto and Pinto 1973) is a uniaxial nonlinear hysteretic constitutive model for carbon steel (reinforcing steel in structural concrete members as well as structural steel sections). This model has been implemented into Open System for Earthquake Engineering Simulation (OpenSees) software (McKenna et al. 2000) as STEEL02 command and is characterised by 10 time-invariant material parameters: E_0, $\sigma_{0.2}$, b, R_0, cR_1, cR_2, α_1, α_2, α_3 and α_4. Particularly, E_0 is the initial Young's modulus, $\sigma_{0.2}$ is the yield stress, b is the post-yield hardening ratio, R_0 is the initial curvature between elastic and post-yield slope, cR_1 is curvature variation parameter of Bauschinger curve after each strain reversal, cR_2 is the curvature variation parameter of Bauschinger curve after each strain reversal, α_1 and α_2 are the isotropic hardening parameters defining stress shift in compression, and α_3 and α_4 are the isotropic hardening parameters defining stress shift in tension.

The material model is expressed in the form of normalised stress–strain relationship as described in Eq. (2) (Giuffrè 1970).

$$\sigma^* = b\varepsilon^* + \frac{(1-b)\varepsilon^*}{\left(1+\left|\varepsilon^*\right|^R\right)^{\frac{1}{\pi}}} \tag{2}$$

where σ^* and ε^* are the normalised stress and strain given from the Eqs. (3) and (4), respectively.

$$\varepsilon^* = \frac{\varepsilon - \varepsilon_r}{\varepsilon_0 - \varepsilon_r} \tag{3}$$

$$\sigma^* = \frac{\sigma - \sigma_r}{\sigma_0 - \sigma_r} \tag{4}$$

The material model employs two linear asymptotes with a smooth transition to simulate the stress for a given strain demand. One asymptote is a line with slope E_0 for the elastic region and the other with a slope $E_1 = b \cdot E_0$ for the post-yield region. As shown in Fig. 10, the linear asymptotes are recalculated for each load reversal, starting from the reversal point for the elastic asymptote (ε_r, σ_r) and crossing the post-yield asymptote at the newly determined yield point. (ε_0, σ_0).

The parameter R of the model defines the curvature of the smooth transition curve between the two linear asymptotes and is updated at each strain reversal. Particularly, R is dependent on the strain amplitude between the latest yield point and the maximum plastic strain in the loading direction after the reversal and is given as follows:

$$R = R_0 \cdot \left(1 - \frac{cR_1 \cdot \xi}{cR_2 + \xi}\right), \quad R(\xi) > 0 \tag{5}$$

where ξ is the normalized plastic strain, which controls R and is defined by Eq. (6).

$$\xi = \left| \frac{\varepsilon_p - \varepsilon_0}{\varepsilon_{0.2}} \right| \tag{6}$$

where ε_p is the maximum logged strain history in the loading direction following the reversal at ε_r, ε_0 is the present yield strain updated after the reversal at ε_r as shown in Figs. 10 and 11, and $\varepsilon_{0.2}$ is the initial yield strain.

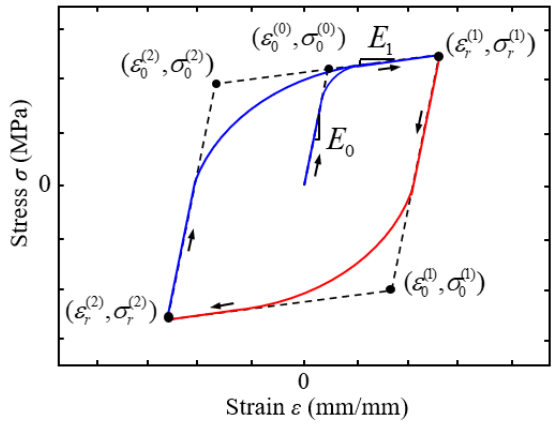

Fig. 10. Update of linear asymptotes at strain reversal points.

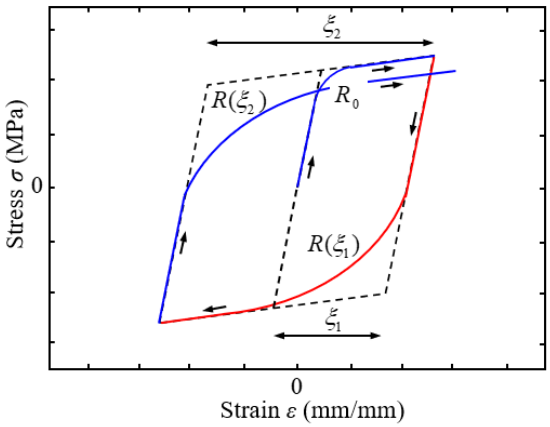

Fig. 11. Definition of $R(\xi)$.

The coordinates of the yield point (ε_0, σ_0) in the (ε, σ) plane depends on the preceding strain reversal point (ε_r, σ_r) and the isotropic hardening effect. The isotropic hardening is accounted in this material model by shifting the post-yield linear asymptote by a stress σ_{st} as shown in Fig. 12.

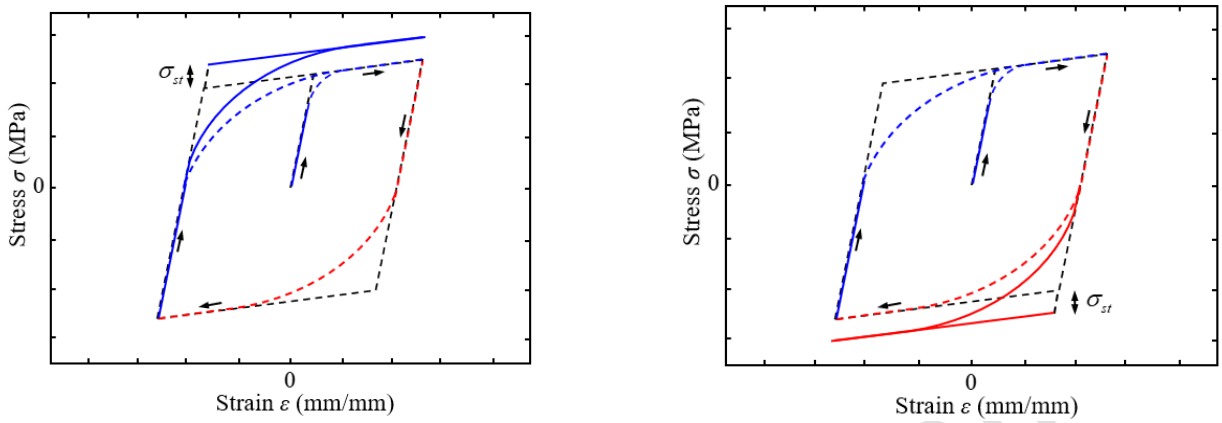

Fig. 12. Stress shift of hardening asymptote; (a) isotropic hardening in compression ($\alpha_1 \neq 0$) and (b) isotropic hardening in tension ($\alpha_3 \neq 0$).

STEEL02 employs a set of equations to consider isotropic hardening for both loading directions. Particularly, Eqs. (7) and (8) provide the stress shift in tension and compression, respectively.

$$\sigma_{st} = \sigma_{0.2} \cdot a_3 \cdot \left(\frac{\varepsilon_p^{\max} - \varepsilon_p^{\min}}{2 \cdot a_4 \cdot \varepsilon_{0.2}} \right)^{0.8} = \frac{a_3}{(a_4)^{0.8}} \cdot \sigma_{0.2} \cdot \left(\frac{\varepsilon_p^{\max} - \varepsilon_p^{\min}}{2 \cdot \varepsilon_{0.2}} \right)^{0.8} \tag{7}$$

$$\sigma_{st} = \sigma_{0.2} \cdot a_1 \cdot \left(\frac{\varepsilon_p^{\max} - \varepsilon_p^{\min}}{2 \cdot a_2 \cdot \varepsilon_{0.2}} \right)^{0.8} = \frac{a_1}{(a_2)^{0.8}} \cdot \sigma_{0.2} \cdot \left(\frac{\varepsilon_p^{\max} - \varepsilon_p^{\min}}{2 \cdot \varepsilon_{0.2}} \right)^{0.8} \tag{8}$$

Where $\varepsilon_p^{\max}$ and $\varepsilon_p^{\min}$ are the maximum and minimum logged strains in each loading direction.

The STEEL02 material model has a different isotropic hardening than the original model defined by Filippou et al. (1983), which suggests a single equation for the stress shift in both loading directions [Eq. (9)].

$$\sigma_{st} = \max\left(\sigma_{0.2} \cdot a_1 \cdot \left(\frac{\varepsilon_{\max}}{\varepsilon_{0.2}} - a_2 \right), 0 \right) \tag{9}$$

where a_1 and a_2 are the isotropic hardening parameters in the original formulation. In this equation, the stress shift depends on the maximum strain in absolute value in either direction as described in Eq. (10).

$$\varepsilon_{\max} = \max\left(\left| \varepsilon_p^{\max} \right|, \left| \varepsilon_p^{\min} \right| \right) \tag{10}$$

Unlike STEEL02 formulations (Eqs. (6) and (7)), Filippou et al. (1983) formulation defines the onset of isotropic hardening, with a specified minimum ductility using the parameter a_2 .

Optimization algorithm

At first stage, the GMP material model was calibrated to reproduce the monotonic stress–strain response of the aluminum alloys considered herein. Particularly, the stress–strain curves obtained from coupons tested under monotonic tensile loading were utilised to calibrate the material parameters *b* and R_0. A normalised least-squares error optimisation was used to minimise the discrepancy between the experimental and predicted material monotonic stress–strain response as described in Eq. (11).

$$error(x) = \sqrt{\frac{\sum_{i=1}^{n}\left(\sigma_e^{(i)} - \sigma_p^{(i)}(x)\right)^2}{\sum_{i=1}^{n}\left(\sigma_e^{(i)}\right)^2}} \tag{11}$$

where $\sigma_e^{(i)}$ is the experimentally obtained stress at the ith strain step, *x* is a vector that holds the parameters of the material model and $\sigma_p^{(i)}(x)$ is the predicted stress at the ith strain step.

The analyses for calibration of the parameters were carried out using MATLAB's Optimization Toolbox (version 2022b) (MathWorks Inc. 2022) following the same methodology reported by Carreño et al. (2019).

Model calibration results

The parameter calibration analyses conducted on each stress–strain response resulted in average fit error, as defined by Eq. (11), of 6.5%, 0.2% and 0.2% for 6082-T6, 6063-T6 and 6060-T5 aluminum alloys, respectively. The achieved fit and the corresponding error level are shown in Figs. 13–15 where the experimental and predicted stress–strain responses are plotted together. It should be noted that the degree of nonlinearity depends mainly on the chemical composition of the alloy and the manufacturing process. Therefore, the experimental stress–strain curves for the same aluminum alloy exhibit a similar degree of nonlinearity, and thus almost the same fit error. While the GMP model provides overall an accurate representation of the monotonic stress–strain response, comparisons between the experimental and predicted stress–strain responses for the different alloys reveals a limitation of this model and particularly its inability to capture the more pronounced hardening behaviour of the 6082-T6 alloy. The

average values and the corresponding coefficients of variation (COVs) of the calibration process for the material model parameters, i.e., E_0, σ_y, b and R_0 for each studied alloy are summarised in Table 3.

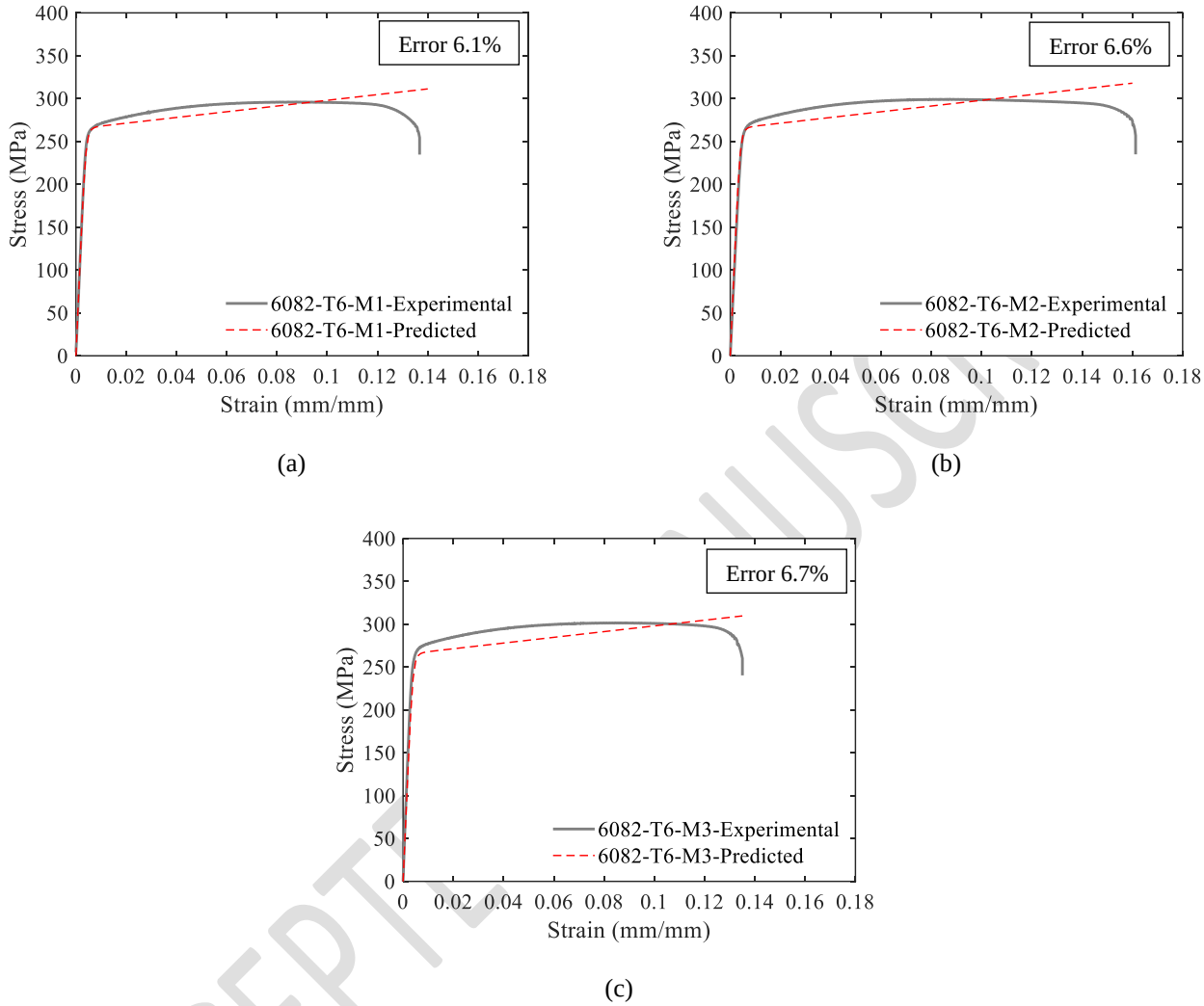

Fig. 13. Comparison between experimental and predicted monotonic stress–strain responses for 6082-T6 aluminum alloy.

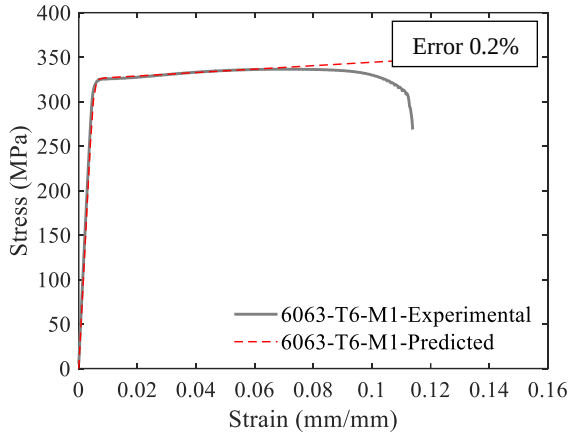

(a)

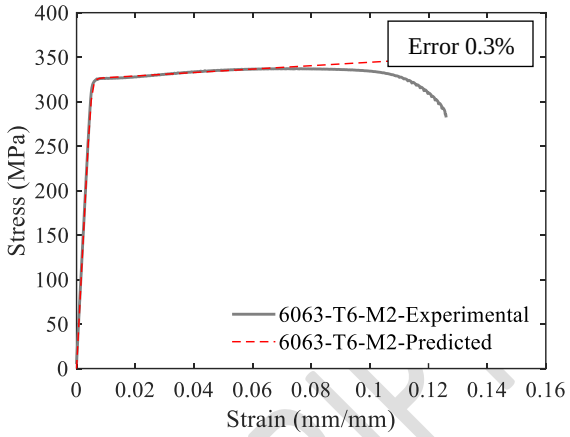

(b)

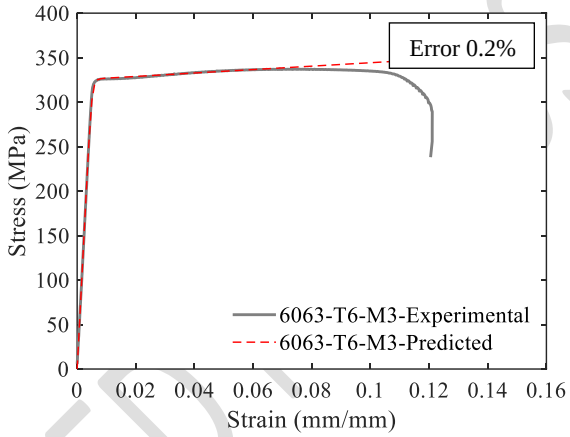

(c)

Fig. 14. Comparison between experimental and predicted monotonic stress–strain responses for 6063-T6 aluminum alloy.

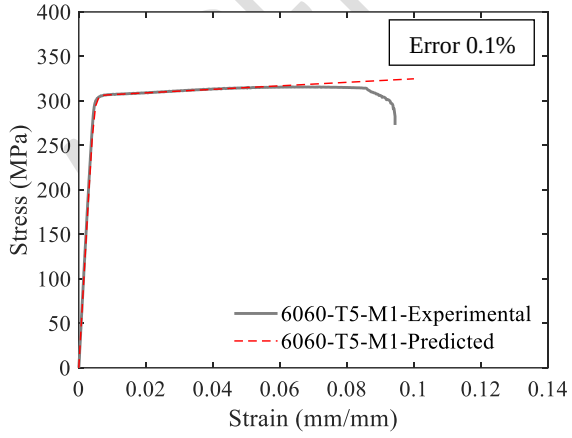

(a)

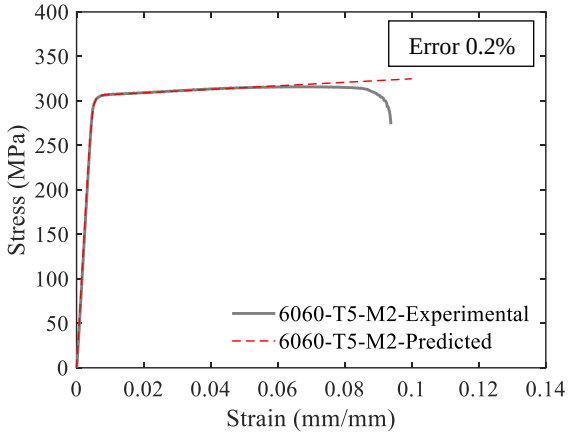

(b)

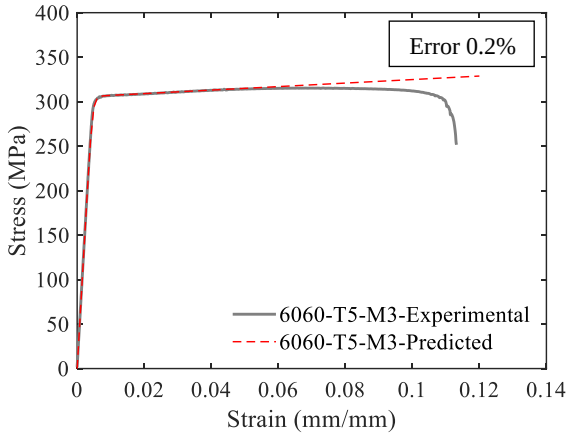

(c)

Fig. 15. Comparison between experimental and predicted monotonic stress–strain responses for 6060-T5 aluminum alloy.

Several observations can be made from the results reported in Table 3 for each calibrated parameter. However, the statistical significance of these results is limited, given the small number of specimens tested per aluminum alloy (3 coupons). For example, the yield stress $\sigma_{0.2}$ shows small variability within each alloy with maximum COV of only 0.8%. However, the $\sigma_{0.2}$ values amongst the studied alloys differ owing to different chemical compositions and production process. In case of Young's modulus E, there is also a very small variability within each aluminum alloy with maximum COV of only 7.9%. Moreover, the average value of E is almost identical amongst the three alloys, with only 3.8% difference between the two extreme alloys namely 6082-T6 and 6063-T6. The post-yield strain hardening ratio b displays consistency for each alloy with value of 0.005 for 6082-T6 alloy and 0.003 for both 6063-T6 and 6060-T5 alloys. The slight difference between the two values results from the more pronounced post-yield strain hardening behaviour of the 6082-T6 alloy. Moreover, the parameter R_0 which controls the curvature of the smooth transition curve between the elastic and plastic branch appears to be higher for both 6063-T6 and 6060-T5 alloys. This is in line with the corresponding experimentally obtained stress–strain curves which display lower degree of roundedness with a sharper yield point compared to those obtained for 6082-T6 alloy. This observation is also reflected by the value of the strain hardening exponent n reported in Table 2, with higher values signifying a less rounded response.

Table 3 Average values and COVs of calibrated GMP model parameters for the monotonic stress–strain response.

Aluminum Alloy	E_0 (MPa) (COV)	σ_y (MPa) (COV)	b (COV)	R_0 (COV)
6082-T6	66634 (7.9%)	266 (0.8%)	0.005 (0.0%)	7.5 (0.0%)
6063-T6	64176 (2.4%)	326 (0.1%)	0.003 (0.0%)	8.5 (0.0%)
6060-T5	65797 (1.8%)	306 (0.0%)	0.003 (0.0%)	8.5 (0.0%)

Modeling of nonlinear stress–strain behaviour under cyclic loading

At second stage, the GMP material model parameters, i.e., E_0, σ_y, b, R_0, cR_1, cR_2, α_1, α_2, α_3, α_4 and *sigInit*, were calibrated based on the stress–strain curves obtained from the cyclic coupon tests. The parameter calibration was performed adopting the same methodology for the parameter calibration analyses for the monotonic tensile response. The resulting average fit error is 5.2%, 4.0% and 4.2% for the 6082-T6, 6063-T6 and 6060-T5 aluminum alloys, respectively. Figs. 16–18 illustrate the experimental and predicted hysteretic responses in the same graph for each coupon specimen along with the achieved error level. Graphical comparisons between the experimental and predicted hysteretic curves denote some of the merits of the GMP model among which are the ability to capture the material strain hardening behaviour and the realistic unloading-reloading behaviour. Overall, it can be concluded that the GMP material model is capable of precisely replicating the hysteretic behaviour of aluminum alloys. Table 4 summarises the average values along with the corresponding COVs of the model parameters, i.e., cR_1, cR_2, α_1, α_2, α_3, α_4 and *sigInit*, resulted from the calibration process for each studied alloy. It is noted that the E_0, σ_y, b *and* R_0 parameters are the same with those resulted from the calibration process of the monotonic stress–strain response (Table 3).

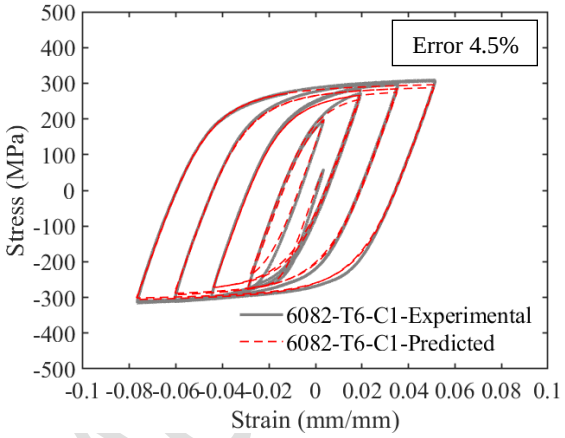

(a)

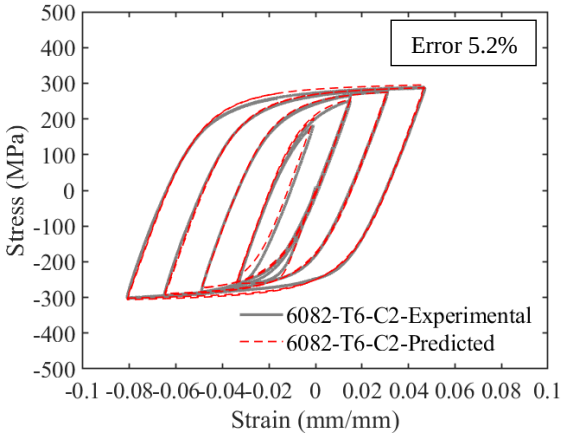

(b)

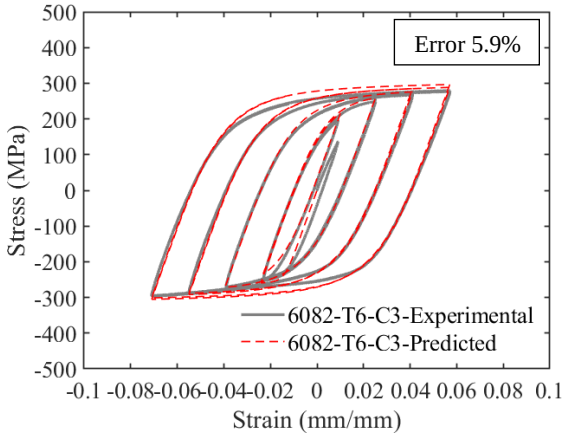

(c)

Fig. 16. Comparison between experimental and predicted hysteretic stress–strain responses for 6082-T6 aluminum alloy.

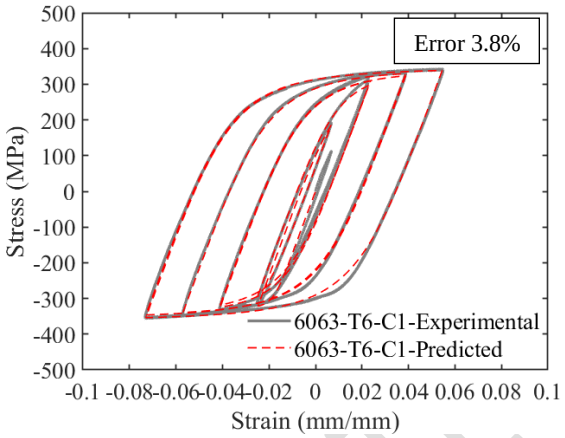

(a)

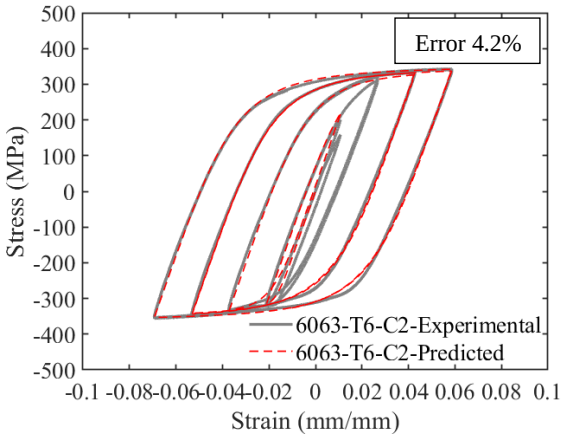

(b)

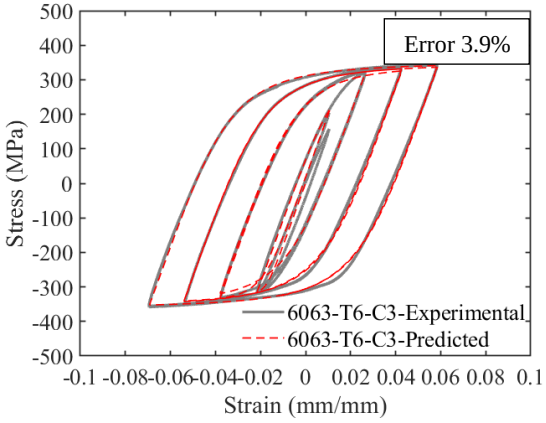

(c)

Fig. 17. Comparison between experimental and predicted hysteretic stress–strain responses for 6063-T6 aluminum alloy.

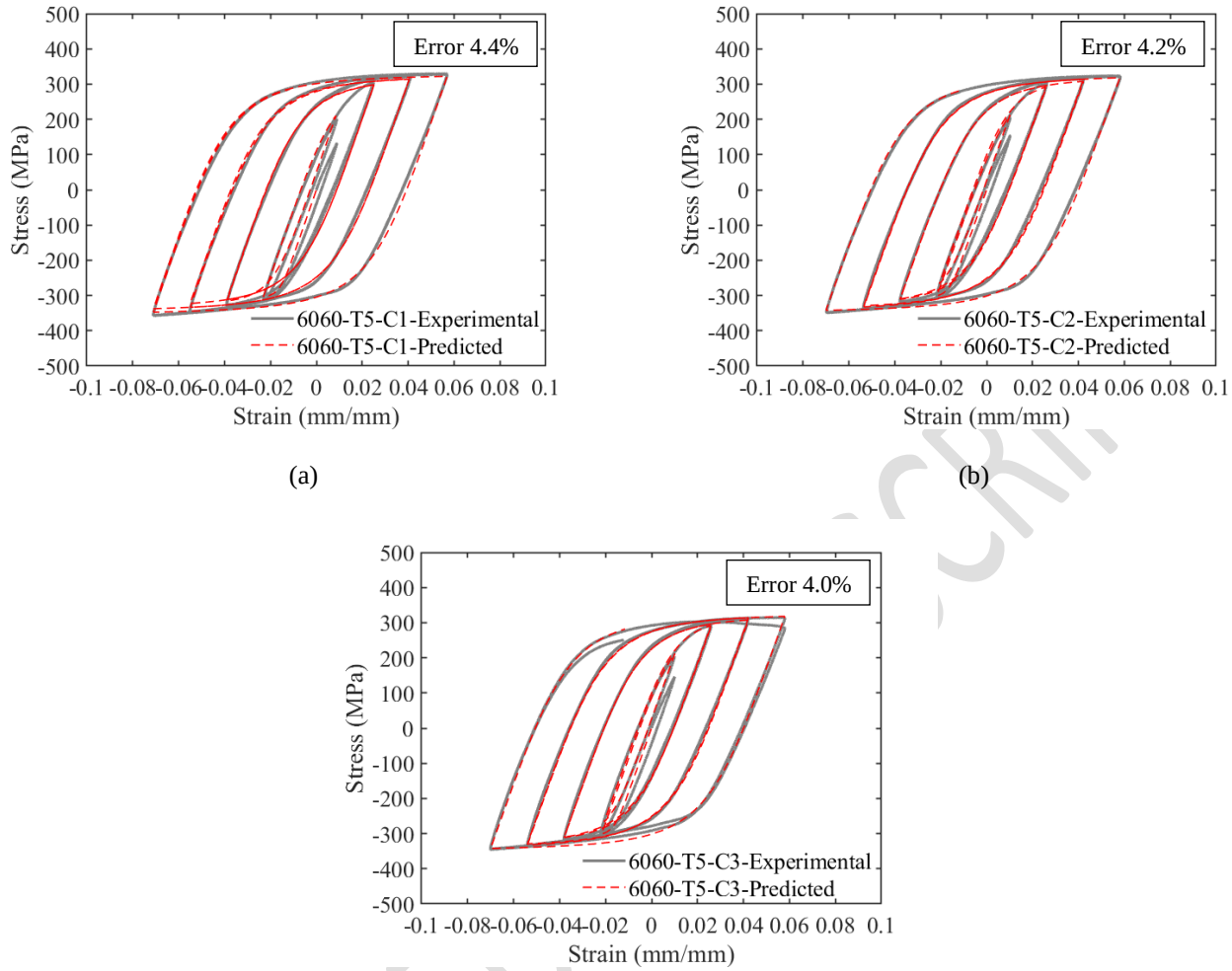

Fig. 18. Comparison between experimental and predicted hysteretic stress–strain responses for 6060-T5 aluminum alloy.

From Table 4 it can be seen that the calibrated model parameters cR_1 and cR_2 which control the curvature of the Bauschinger curve were found to be constant and equal to 0.6 and 0.15 for all aluminum alloys. The parameter controlling the isotropic hardening α_1 has variability within the alloys with maximum COV of 12.3%. The second parameter controlling the isotropic hardening α_3 exhibits the largest variability with 29.7% maximum COV. It is noteworthy that all tested coupons exhibited larger isotropic hardening in compression than in tension which compensates for the increased cross-sectional area of the coupon specimen in compression.

Table 4 Average values of calibrated GMP model parameters for the hysteretic stress–strain response.

Aluminum Alloy	R_0 (COV)	cR_1 (COV)	cR_2 (COV)	a_1 (COV)	a_2 (COV)	a_3 (COV)	a_4 (COV)
6082-T6	7.5 (0%)	0.6 (0%)	0.15 (0%)	0.051 (8.3%)	1 (0%)	0.042 (24.9%)	1 (0%)
6063-T6	7.5 (0%)	0.6 (0%)	0.15 (0%)	0.035 (0%)	1 (0%)	0.020 (0%)	1 (0%)
6060-T5	7.5 (0%)	0.6 (0%)	0.15 (0%)	0.046 (12.3%)	1 (0%)	0.021 (29.7%)	1 (0%)

Model implementation and verification

The modified model proposed in this paper was implemented into OpenSees using the uniaxial material model STEEL02 command and adopting the calibrated parameters for monotonic stress–strain response listed in Table 3. The bare aluminum tubular (BAT) columns reported by Georgantzia et al. (2021b) were utilised to verify the accuracy and reliability level of this model. A total of 9 6082-T6 aluminum alloy square and rectangular pin-ended columns were tested under concentric compression as shown in Fig. 19 and the predominant failure mode was flexural buckling. Finite element modeling was also performed and was successfully validated against the experimental results.

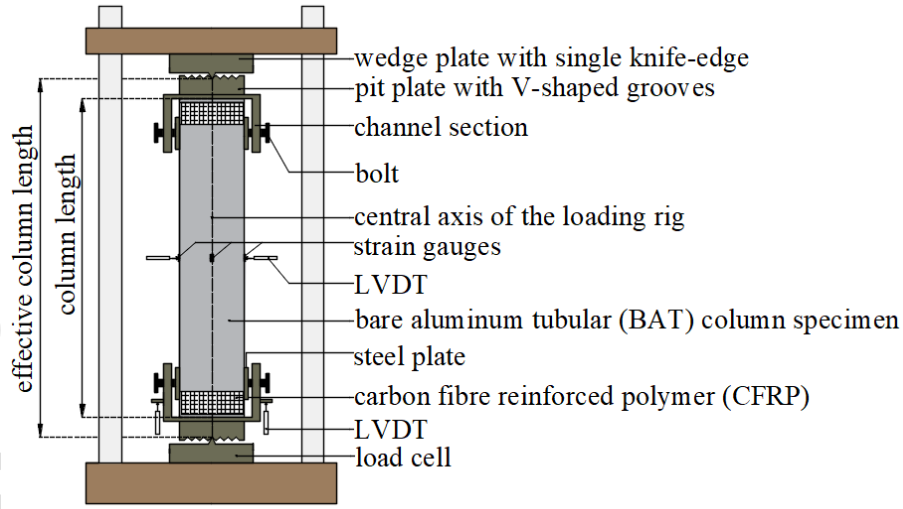

Fig. 19. Experimental set-up of flexural buckling tests reported by Georgantzia et al. (2021b).

Nonlinear fiber element modeling assumptions

A study employing fiber-based modeling was conducted, where each column was constructed using unidirectional aluminum fibers. These fibers were assumed to follow a specific stress–strain relationship outlined by Spacone et al.

(1996). The strain of each fiber is calculated based on the section deformation, considering the plane section assumption. Subsequently, the fiber strain and stress were updated according to the corresponding material model, followed by adjustments to the section force resultant and the corresponding stiffness (Zhao and Sritharan 2007).

A two-dimensional non-linear model was developed for each tested column, as depicted in Fig. 20, utilizing the measured geometric properties prior to the tests. The models were constructed using the *non-linearBeamColumn* element, which accounts for the spread of plasticity along the length of the element (Mazzoni et al. 2006). Pin-ended boundary conditions were defined based on the effective length of the specimens measured during the tests. The top and bottom nodes were restrained against all translational degrees of freedom, except the longitudinal translation at the loaded end, while rotational movement about the examined buckling axis was allowed.

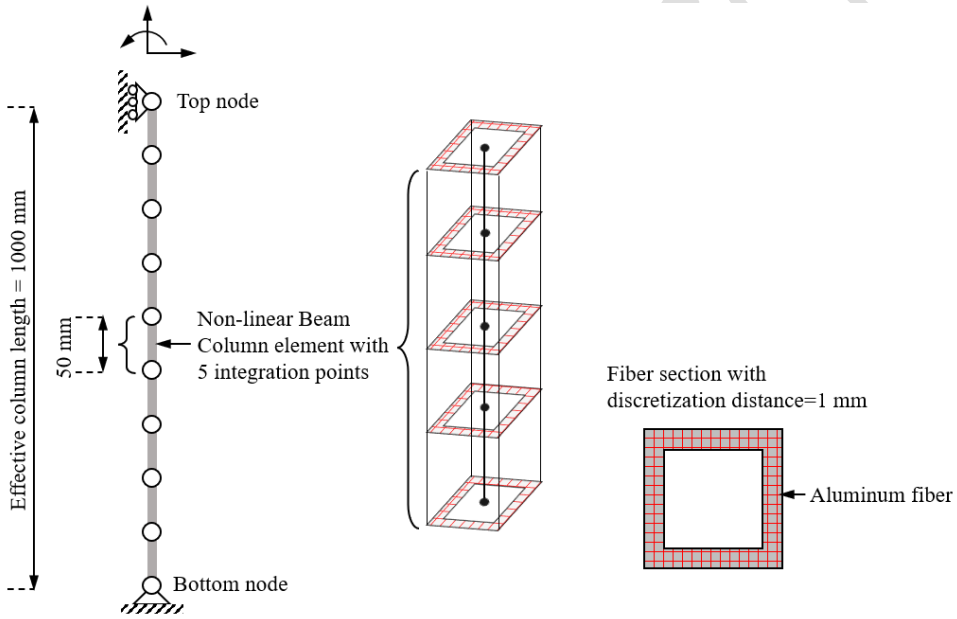

Fig. 20. Overview of fiber element modeling.

It is well-established that the compressive behavior of thin-walled columns is significantly influenced by initial geometric imperfections (Chen et al. 2017; Georgantzia and Gkantou 2021; Georgantzia et al. 2021c, 2023). To account for this, the initial geometry of the column was perturbed using a Fourier sine series (Eq. 12), aligning with the experimental failure mode shape.

$$\omega_g(x)_i = \frac{L}{1000}\sin\frac{\pi x}{L} \tag{12}$$

where ω_g is the global imperfection amplitude at node *i*, *L* is the column length and *x* is the distance of the node *i* from the bottom of the column as shown in Fig. 21.

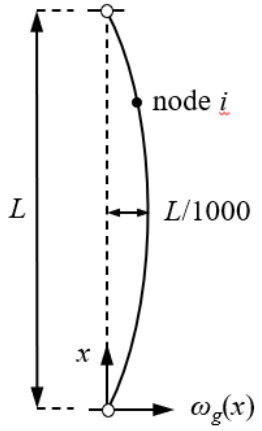

Fig. 21. Schematic of initial global imperfections of a pin-ended column.

The global imperfection amplitude was set equal to the 1/1000 of the critical buckling length as this value was found to provide the best agreement between the tests and finite element modeling results. However, the formulation of the *non-linearBeamColumn element* is not amenable to the inclusion of local buckling, and thus the initial local geometric imperfections were not accounted for (Chen 2010). A sensitivity analysis was conducted to identify the optimal number of elements and fibers that could maintain accuracy while capturing the behavior under geometric and material nonlinearities. The column model, with a length of 1000 mm, was discretized into 20 elements, and a fiber section discretization distance of 1 mm was applied. The material modeling parameters (E_0 and σ_y) were set in accordance with experimental values, while the *b* and R_0 values were derived from Table 3. Residual stresses resulting from the heat treatment of the 6082-T6 alloy, as confirmed by Mazzolani (1975), were considered negligible and thus disregarded in this study. To replicate the loading conditions used in the tests, a concentric compressive load was applied at the top node by specifying a displacement. A nonlinear analysis utilizing the Newton-Raphson algorithm was conducted to comprehensively capture the columns' nonlinear response.

In Fig. 22 the compressive capacities obtained from fiber element modeling $N_{u,FibE}$ are plotted against those resulted from experiments $N_{u,Exp}$ and finite element modeling $N_{u,FinE}$. As can be seen the mean value of $N_{u,FibE}/N_{u,Exp}$ ratios is 0.96 and the corresponding COV is 0.05 which suggest quite accurate and consistent numerical predictions. Moreover, the mean value of the $N_{u,FibE}/N_{u,FinE}$ ratios is close to unity showing that there is a fairly good agreement between the results obtained from fiber and finite element modeling. The same conclusions can be derived from Fig.

23 where the experimental and numerical load–mid-height lateral displacement curves for the 50.8×50.8×3.3 and 76.2×38.1×3.3 columns are plotted together. Fig. 24 presents for the same columns the experimental and numerical load–in-plane normal strains at the mid-height verifying further the developed fiber element models. It is noted that tension is positive, and compression is negative in these graphs. In modeling nonlinear buckling and post-buckling behavior of metallic structural members constitutive material model should be able to capture the cyclic loading and unloading behavior of buckled section accurately. As it is evident in Fig. 24 the normal strain on outer face of the column is initially in compression, but it is reversing to tension in post-buckling region. This is due the influence of second order effect that imposes additional moment at the buckled section. Therefore, if the material model cannot capture this load reversal accurately, it will affect the performance prediction of the structural components. This is particularly important to model nonlinear behavior of structures subject to earthquake cyclic loading. The experimental results show that the proposed modified material model is able to capture this phenomenon. Overall, the comparisons demonstrate that the fiber element models developed adopting the assumptions set above can capture effectively the experimental initial stiffness, compressive capacity and post-buckling response. There is a need for additional experimental testing on aluminum sections under cyclic loading for further verification of the proposed model, nevertheless, the proposed model paves the way for future research in this area.

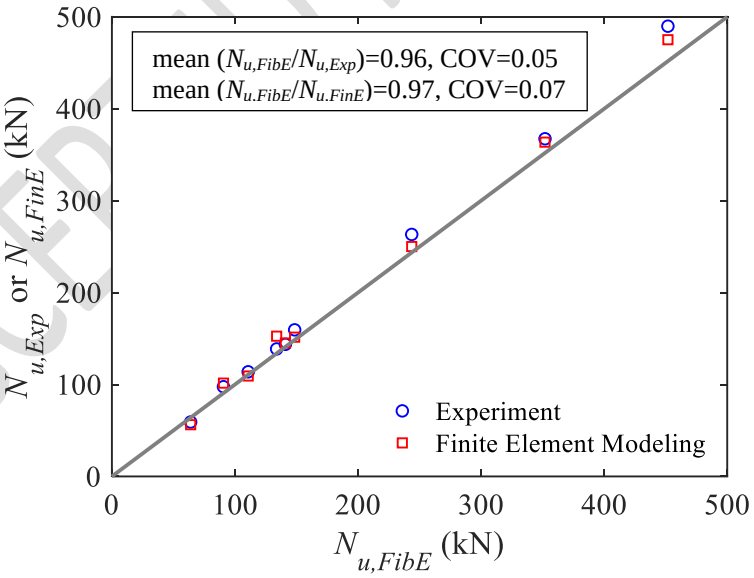

Fig. 22. Comparison between experimental and numerical compressive capacities.

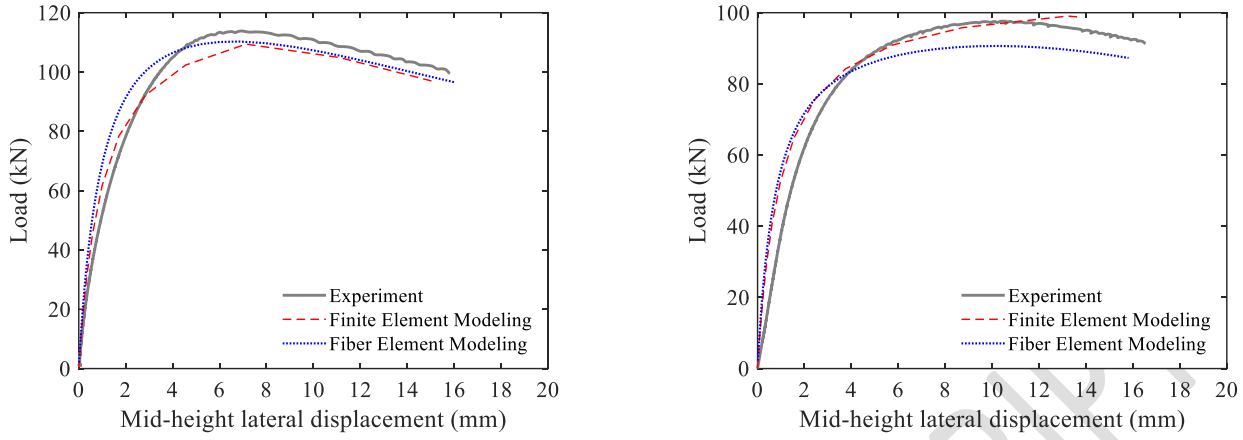

Fig. 23. Comparison between experimental and numerical load–mid-height lateral displacement curves; (a) 50.8×50.8×3.3 and (b) 76.2×38.1×3.3 columns.

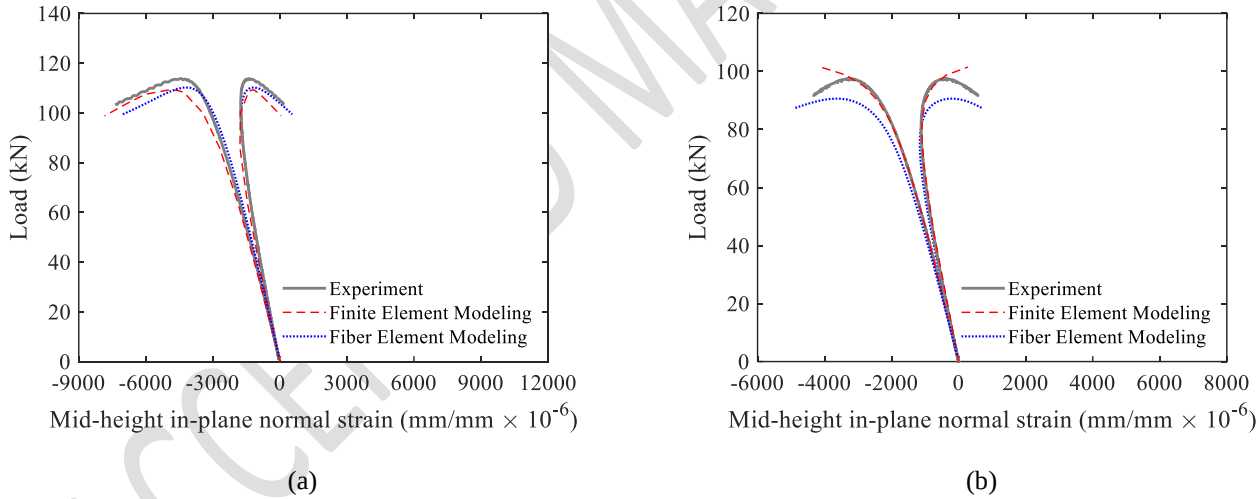

Fig. 24. Comparison between experimental and numerical load–in-plane normal strains at the mid-height; (a) 50.8×50.8×3.3 and (b) 76.2×38.1×3.3 columns.

Conclusions

The purpose of this study was to evaluate the cyclic behaviour and hysteretic energy dissipation capacity of 6000 series aluminum alloys and develop a nonlinear hysteretic constitutive model. For this purpose, tensile, and cyclic tests were conducted on coupons made from 6082-T6, 6063-T6 and 6060-T5 aluminum alloys up to 6.5% strain amplitude. The following conclusions can be drawn from the results of this work:

(1) At increased strain demands under cyclic loading the investigated aluminum alloys exhibited isotropic hardening behaviour without cyclic material degradation.

(2) The 6082-T6 which is the most ductile alloy, presents higher hysteretic energy dissipation capacity by 1.34 and 1.58 times more than 6063-T6 and 6060-T6 alloys, respectively.

(3) A modified Giuffrè-Menegotto-Pinto constitutive model for the nonlinear stress–strain behaviour under cyclic loading was suggested based on the experimental results. The average fit error is 5.2%, 4.0% and 4.2% for 6082-T6, 6063-T6 and 6060-T5 aluminium alloys, respectively. This shows that the proposed model is able to capture the material strain hardening behaviour and the realistic unloading-reloading behaviour.

(4) Verified calibrated Giuffrè-Menegotto-Pinto model parameters for prediction of the nonlinear stress–strain behaviour under monotonic tensile loading were also recommended. Fiber element modeling study on the flexural buckling performance of 6082-T6 aluminum alloy columns was performed to verify further the recommended values. The obtained data were compared with those from experimental and finite element modeling studies in the literature showing that the proposed parameters provide reasonably accurate results with good consistency.

Overall, this research study provides evidence about the 6000 series aluminum alloys' hysteretic behaviour and thus their potential for deployment in structural applications in earthquake prone areas. It also suggests a modified Giuffrè-Menegotto-Pinto constitutive model for the nonlinear stress–strain behaviour under monotonic tensile and cyclic loading which could be implemented into commonly-used open-source OpenSees software for numerical modeling of aluminum alloy structures. However, more research studies are required to validate further the accuracy and reliability level of the proposed constitutive model.

Acknowledgements

The authors would like to thank the technicians of the Department of Civil, Maritime and Environmental Engineering at University of Southampton for their valuable assistance and support.

Data Availability Statement

Some or all data, models, or code that support the findings of this study are available from the corresponding author upon reasonable request.

References

"aalco, The UK's largest independent multi-metals stockholder." 2022. Accessed April 21, 2023. https://www.aalco.co.uk/.

American Society for Testing and Materials. 2017. *ASTM E606-04: Standard Practice for Strain-Controlled Fatigue Testing*. *ASTM International*.

Baehre, R. 1966. "Trycktastravorav elastoplastikt material-nagrafragestallningar (Comparison between structural behaviour of elastoplastic materials)." *Tekn Arne Johnson Ingenjorsbyra*.

Carreño, R., C. Carreño, S. M. Asce, ; K H Lotfizadeh, ; J P Conte, M. Asce, and J. I. Restrepo. 2019. "Material Model Parameters for the Giuffrè-Menegotto-Pinto Uniaxial Steel Stress-Strain Model." https://doi.org/10.1061/(ASCE).

Chaboche, J. L. 1989. "Constitutive equations for cyclic plasticity and cyclic viscoplasticity." *Int J Plast*, 5 (3): 247–302. https://doi.org/10.1016/0749-6419(89)90015-6.

Chen, C. 2010. "Performance-Based Seismic Demand Assessment of Concentrically Braced Steel Frame Buildings." UC Berkeley.

Chen, Y., R. Feng, and J. Xu. 2017. "Flexural behaviour of CFRP strengthened concrete-filled aluminium alloy CHS tubes." *Constr Build Mater*, 142: 295–319. https://doi.org/10.1016/j.conbuildmat.2017.03.040.

Dusicka, P., and J. Tinker. 2013. "Global Restraint in Ultra-Lightweight Buckling-Restrained Braces." *Journal of Composites for Construction*, 17 (1): 139–150. American Society of Civil Engineers (ASCE). https://doi.org/10.1061/(asce)cc.1943-5614.0000320.

European Committee for Standardization (CEN). 2009. *Metallic Materials – Tensile Testing – Part 1: Method Of Test At Room Temperature*. *Brussels*.

Filippou, F., E. Popov, and V. Bertero. 1983. *Effects of Bond Deterioration on Hysteretic Behavior of Reinforced Concrete Joints*. Washington, DC.

Georgantzia, E., S. Bin Ali, M. Gkantou, G. S. Kamaris, K. D. Kansara, and W. Atherton. 2021a. "Flexural buckling performance of concrete-filled aluminium alloy tubular columns." *Eng Struct*, 242. https://doi.org/10.1016/j.engstruct.2021.112546.

Georgantzia, E., and M. Gkantou. 2021. *Flexural Buckling of Concrete-Filled Aluminium Alloy CHS Columns: Numerical Modelling and Design*. *Lecture Notes in Civil Engineering*.

Georgantzia, E., M. Gkantou, and G. S. Kamaris. 2021b. "Aluminium alloys as structural material: A review of research." *Eng Struct*, 227. https://doi.org/10.1016/j.engstruct.2020.111372.

Georgantzia, E., M. Gkantou, and G. S. Kamaris. 2021c. "Numerical Modelling and Design of Aluminium Alloy Angles under Uniform Compression." *CivilEng*, 2 (3). https://doi.org/10.3390/civileng2030035.

Georgantzia, E., M. Gkantou, and G. S. Kamaris. 2023. "Aluminium alloy channel columns: Testing, numerical modelling and design." *Thin-Walled Structures*, 182. https://doi.org/10.1016/j.tws.2022.110242.

Georgantzia, E., M. Gkantou, G. S. Kamaris, and K. D. Kansara. 2022a. "Design of aluminium alloy channel sections under minor axis bending." *Thin-Walled Structures*, 174. https://doi.org/10.1016/j.tws.2022.109098.

Georgantzia, E., M. Gkantou, G. S. Kamaris, and K. D. Kansara. 2022b. "Ultimate response and plastic design of aluminium alloy continuous beams." *Structures*, 39. https://doi.org/10.1016/j.istruc.2022.03.015.

Giuffrè, A. 1970. "Il comportamento del cemento armato per sollecitazioni cicliche di forte intensità." *Giornale del Genio Civile*, 28: 1–20.

Guo, X., Z. Shen, Y. Li, C. Su, Z. Qiu, and N. Yao. 2007. "Stress-strain relationship and physical-mechanical properties of domestic structural aluminum alloy." *Jianzhu Jiegou Xuebao/Journal of Building Structures*, 28: 110–117.

Guo, X., L. Wang, Z. Shen, J. Zou, and L. Liu. 2018. "Constitutive model of structural aluminum alloy under cyclic loading." *Constr Build Mater*, 180: 643–654. Elsevier Ltd. https://doi.org/10.1016/j.conbuildmat.2018.05.291.

Hill, H. N., J. W. Clark, and R. J. Brungraber. 1960. "Design of Welded Aluminum Structures." *Journal of the Structural Division*, 86 (6): 101–124. https://doi.org/10.1061/JSDEAG.0000524.

Hopperstad, O. S., M. Langseth, and S. Remseth. 1995a. “Cyclic stress-strain behaviour of alloy AA6060, part I: Uniaxial experiments and modelling.” *Int J Plast*, 11 (6): 725–739. https://doi.org/10.1016/S0749-6419(95)00032-1.

Hopperstad, O. S., M. Langseth, and S. Remseth. 1995b. “Cyclic stress-strain behaviour of alloy AA6060 T4, part II: Biaxial experiments and modelling.” *Int J Plast*, 11 (6): 741–762. https://doi.org/10.1016/S0749-6419(95)00033-X.

Kashani, M. M., A. J. Crewe, and N. A. Alexander. 2013. “Nonlinear cyclic response of corrosion-damaged reinforcing bars with the effect of buckling.” *Constr Build Mater*, 41: 388–400. https://doi.org/10.1016/j.conbuildmat.2012.12.011.

Kaufman, J. G. (John G. 2000. *Introduction to aluminum alloys and tempers*. ASM International.

Mander, J. B., F. D. Panthaki, and A. Kasalanati. 1994. “Low-Cycle Fatigue Behavior of Reinforcing Steel.” *Journal of Materials in Civil Engineering*, 6 (4): 453–468. https://doi.org/10.1061/(ASCE)0899-1561(1994)6:4(453).

De Matteis, G., G. Brando, and F. M. Mazzolani. 2012. “Pure aluminium: An innovative material for structural applications in seismic engineering.” *Constr Build Mater*, 26 (1): 677–686. https://doi.org/10.1016/j.conbuildmat.2011.06.071.

Mazzolani, F. 1975. *Residual Stress Tests Alu-Alloy Austrian Profiles*. ECCS Committee, Brussels .

Mazzoni, S., F. McKenna, M. Scott, and G. Fenves. 2006. “OpenSees command language manual.” Pacific Earthquake Engineering Research (PEER) Center.

Menegotto, M., and P. Pinto. 1973. “Method of analysis for cyclically loaded RC plane frames including changes in geometry and non-elastic behavior of elements under combined normal force and bending.” *IABSE Symposium on Resistance and Ultimate Deformability of Structures Acted on by Well Defined Repeated Loads*, 15–22. Zurich, Switzerland: International Association for Bridge and Structural Engineering.

Nip, K., L. Gardner, C. Davies, and A. Elghazouli. 2010. “Extremely low cycle fatigue tests on structural carbon steel and stainless steel.” *J Constr Steel Res*, 66 (1): 96–110. https://doi.org/10.1016/j.jcsr.2009.08.004.

OpenSees. 2011. “The Open System for Earthquake Engineering Simulation. PEER.” University of California, Berkeley.

Ramberg, W., and W. Osgood. 1943. *Description of stress-strain curves by three parameters. Vol. Technical*. Washington, D.C.: National Advisory Committe for Aeronautics.

Shi, Y., M. Wang, and Y. Wang. 2011. "Experimental and constitutive model study of structural steel under cyclic loading." *J Constr Steel Res*, 67 (8): 1185–1197. https://doi.org/10.1016/j.jcsr.2011.02.011.

Spacone, E., F. Filippou, and F. Taucer. 1996. " Fibre beam-column model for non-linear analysis of R/C frames: part II. applications." *Earthq Eng Struct Dyn*, 25 (7): 711–725. https://doi.org/10.1002/(SICI)1096-9845(199607)25:7<711::AID-EQE576>3.0.CO;2-9.

Steinhardt, P. J., D. R. Nelson, and M. Ronchetti. 1983. "Bond-orientational order in liquids and glasses." *Phys Rev B*, 28 (2): 784–805. https://doi.org/10.1103/PhysRevB.28.784.

The MathWorks Inc. 2022. "Optimization Toolbox version: 9.4 (R2022b)." Accessed May 10, 2023. https://www.mathworks.com.

Yujin, W., F. Feng, Q. Hongliang, and Z. Ximei. 2013. "Experimental study on constitutive model of high-strength aluminum alloy 6082-T6." *Journal of Building Structures*, 34 (6): 113.

Zhao, J., and S. Sritharan. 2007. "Modeling of Strain Penetration Effects in Fiber-Based Analysis of Reinforced Concrete Structures." *ACI Struct J*, 104 (2): 133–141. https://doi.org/10.14359/18525.

Table 1. Nominal chemical composition of the examined aluminum alloys (aalco 2022).

	Aluminum Alloy		
	6082-T6	6063-T6	6060-T5
Element	% Present		
Silicon (Si)	0.70-1.30	0.20-0.60	0.30-0.60
Magnesium (Mg)	0.60-1.20	0.45-0.90	0.35-0.60
Manganese (Mn)	0.40-1.00	0-0.10	0-0.10
Iron (Fe)	0-0.50	0-0.35	0.10-0.30
Chromium (Cr)	0-0.25	0-0.10	0-0.05
Zinc (Zn)	0-0.20	0-0.10	0-0.15
Titanium (Ti)	0-0.10	0-0.10	0-0.10
Copper (Cu)	0-0.10	0-0.10	0-0.10
Others (Each)	0-0.05	0-0.05	0-0.05
Others (Total)	0-0.15	0-0.15	0-0.15
Aluminum (Al)	Balance	Balance	Balance

Table 2 Material properties obtained from monotonic tensile tests.

Specimen	E (MPa)	$\sigma_{0.1}$ (MPa)	$\sigma_{0.2}$ (MPa)	σ_u (MPa)	ε_u (%)	ε_f (%)	n	$\sigma_u/\sigma_{0.2}$
6082-T6-M1	66638	258.2	263.9	296.0	9.18	13.68	31.84	112%
6082-T6-M2	60182	259.8	266.6	299.2	7.93	16.13	26.95	112%
6082-T6-M3	73081	260.6	268.8	301.5	8.43	13.50	22.40	112%
6063-T6-M1	66323	322.0	325.2	336.6	6.99	11.39	69.37	103%
6063-T6-M2	62716	322.9	325.9	337.2	7.50	12.60	74.72	103%
6063-T6-M3	63488	322.8	325.8	337.5	6.90	12.05	75.66	104%
6060-T5-M1	67434	302.0	306.2	315.7	6.80	9.44	50.79	103%
6060-T5-M2	64862	301.5	306.0	315.9	6.79	9.38	46.69	103%
6060-T5-M3	65094	302.4	305.9	315.3	7.34	11.32	60.69	103%

Table 3 Average values and COVs of calibrated GMP model parameters for the monotonic stress–strain response.

Aluminum Alloy	E_0 (MPa) (COV)	σ_y (MPa) (COV)	b (COV)	R_0 (COV)
6082-T6	66634 (7.9%)	266 (0.8%)	0.005 (0.0%)	7.5 (0.0%)
6063-T6	64176 (2.4%)	326 (0.1%)	0.003 (0.0%)	8.5 (0.0%)
6060-T5	65797 (1.8%)	306 (0.0%)	0.003 (0.0%)	8.5 (0.0%)

Table 4 Average values of calibrated GMP model parameters for the hysteretic stress–strain response.

Aluminum Alloy	cR_1 (COV)	cR_2 (COV)	a_1 (COV)	a_2 (COV)	a_3 (COV)	a_4 (COV)
6082-T6	0.6 (0%)	0.15 (0%)	0.051 (8.3%)	1 (0%)	0.042 (24.9%)	1 (0%)
6063-T6	0.6 (0%)	0.15 (0%)	0.035 (0%)	1 (0%)	0.020 (0%)	1 (0%)
6060-T5	0.6 (0%)	0.15 (0%)	0.046 (12.3%)	1 (0%)	0.021 (29.7%)	1 (0%)